PAPER

Check for updates

Chemistry-dependent magnetic properties at the FeNi oxide–metal interface†

F. Genuzio, [ID] ‡*[a] T. O. Menteş, [ID] [a] K. Freindl, [ID] [b] N. Spiridis, [ID] [b] J. Korecki [ID] [bc] and A. Locatelli [ID] [a]

Fe and Ni compounds and their oxides offer stoichiometry-dependent magnetic properties, owing to an extremely rich variety of crystallographic phases and a complex phase diagram. They foster the fabrication of oxide/metal magnetic junctions with tunable coupling, thus avoiding the usage of costly materials such as Co and rare-earth elements. Along these lines, here, spectro-microscopy is employed to study the oxidation of FeNi alloy ultrathin films featuring laterally separated fcc and bcc phases. Under mild oxidation conditions at $T < 250$ °C, Fe segregates to the surface forming a thin superficial Fe-oxide layer, which eventually evolves to Fe_3O_4 supported on an interfacial FeNi oxide with a spinel structure. Notably, the bcc FeNi oxidizes faster than the fcc one, while the fcc/bcc phase boundary is found to be the most reactive surface region. The magnetic coupling and domain morphology of the oxide–metal heterostack, characterized by XMCD-PEEM and CEMS, are shown to depend on the crystallographic structure of the alloy film. In particular, the Fe-oxide layer on top of the fcc regions exhibits micron-sized uniform magnetic domains antiferromagnetically coupled to the metal support. In contrast, the corresponding oxide on the bcc regions displays fragmented magnetic domains at a length scale of about 100 nm, with ferromagnetic coupling to the underlying FeNi metal support. Our study identifies novel principles for engineering the magnetic coupling through the interface structure and chemistry, with potential applications in sustainable spintronics.

1. Introduction

Metal–oxide heterostructures are widely used materials, with prototypical usage in interfacial chemistry and magnetism. In this context, magnetic tunnel junctions and magnetoresistivity,[1,2] control of magnetic anisotropy[3] and subsequent formation of exotic magnetic structures[4] can be considered of particular relevance for metal-oxide interfacial magnetism. In stacked systems, the epitaxial relation and the atomic termination between adjacent layers are particularly important for interface-induced magnetism, as pointed out in a recent review by Hellman *et al.*[5] In artificially fabricated hetero-structures, the presence of structural mismatch, epitaxial strain, atomic defects or intermixing at the layer boundaries might significantly perturb the intrinsic interfacial magnetic properties. On the other hand, this sensitivity can be used to modify, control and tune the properties of magnetic layers *via* the interface structure.[6–8]

Here, we focus on the formation and magnetic coupling of Fe-oxides grown on the Fe–Ni bimetallic alloy with varying stoichiometry, constituting a metal–oxide system with a tunable surface structure and composition. Regarding magnetic oxides, iron oxide has been at the forefront from the very early history of magnetism,[9] to the recent day.[10] It features several phases with various oxidation states and crystalline structures.[11] The controlled growth and transformations of the thin film counterparts of these phases were studied by the authors among others.[12–16] Among all the Fe oxide phases, Fe_3O_4 is the one with the highest interest for magnetic applications, owing to its high Curie temperature and its half-metallic character at RT (room temperature).[11] Hence, Fe_3O_4 thin films are attractive candidates for incorporation in spintronic devices operating at RT as high-spin-polarized electrodes.[8,17–20]

Interestingly, Fe–Ni alloys have outstanding magnetic properties,[21,22] and were exploited for the first demonstration of the ''spin-valve''-like behaviour.[23,24] The Fe–Ni alloys offer several phases with distinct structural and magnetic properties as a function of composition and temperature.[25,26] The alloy magnetization evolves throughout the entire range of compositions, featuring two of the most popular alloys in permalloy ($\approx 80\%$ Ni) and Invar ($\approx 35\%$ Ni).[27] Furthermore, the existence of a miscibility

[a] *Elettra – Sincrotrone Trieste S.C.p.A., Basovizza, Trieste 34149, Italy.*
  E-mail: francesca.genuzio@elettra.eu
[b] *Jerzy Haber Institute of Catalysis and Surface Chemistry, Polish Academy of Sciences, ul. Niezapominajek 8, 30-239 Kraków, Poland*
[c] *AGH University of Science and Technology, Faculty of Physics and Applied Computer Science, al. Mickiewicza 30, 30-259 Kraków, Poland*
† Electronic supplementary information (ESI) available. See DOI: 10.1039/d0tc00311e
‡ Current address: Ceric-Eric SS 14-km 163.5 in Area Science Park 34149 – Basovizza Trieste, Italy. E-mail: francesca.genuzio@ceric-eric.eu

This journal is © The Royal Society of Chemistry 2020

J. Mater. Chem. C, 2020, **8**, 5777–5785 | 5777

gap in the range of about 10%–50% Ni introduces the micro-structure as another aspect of the bimetallic alloy.[26] In particular, the miscibility gap leads to phase separation into micron-sized fcc(111) and bcc(110) regions for Fe–Ni ultrathin films grown on W(110).[28,29]

The oxidation of $Fe_{1-x}Ni_x$ surfaces was reported to result in Fe surface segregation and its selective oxidation in the early literature.[30,31] The current work is built on these observations and is extended to Fe–Ni surfaces showing lateral heterogeneity. Thus, in the following we address the questions: (i) how does the oxidation rate depend on the structure and composition of Fe–Ni; (ii) what is the chemical state of the interface; and (iii) how are the magnetic properties of the oxide–metal system influenced by the symmetry and chemistry at the interface?

The paper first presents the growth of $Fe_{0.7}Ni_{0.3}$ films on W(110) and their subsequent separation into fcc(111) and bcc(110) regions upon annealing. Then, it shows the effect of exposing this surface to varying amounts of oxygen, using complementary surface microscopy and spectroscopy methods. Such characterization demonstrates the formation of a layered oxide/metal structure. In the last part, bearing in mind the potential application for spintronic devices, the magnetic properties and the magnetic coupling between the layers of the resulting oxide–metal composite are discussed.

2. Experimental

The experiments were carried out using the spectroscopic photoemission and low-energy electron microscopy (SPELEEM) instrument at the Nanospectroscopy beamline at Elettra (Trieste, Italy)[32] and a conversion electron Mössbauer spectroscope (CEMS) at the Jerzy Haber Institute of Catalysis and Surface Chemistry Polish Academy of Sciences (Krakow, Poland).[12]

The SPELEEM instrument combines X-ray photoemission electron microscopy (XPEEM) with low-energy electron microscopy (LEEM). The former provides laterally resolved chemical and magnetic information, whereas the latter is a structural probe mostly applied to crystalline surfaces.[33,34] In this SPELEEM microscope, the lateral resolution is about 30 nm in XPEEM, and it reaches 10 nm in the LEEM mode.[35] In addition to real space imaging, the microscope can also perform diffraction measurements by imaging the backfocal plane of the objective lens. In the case of elastic backscattering of incident electrons, this allows a measurement of low-energy electron diffraction with a micron-sized probed area (μ-LEED).

The nanospectroscopy beamline boasts two Apple II type undulators, which provide linearly and circularly polarized soft X-rays to the SPELEEM microscope in the energy range from 25 eV up to about 1000 eV.[32,35] The circular polarization is used in order to image magnetic domains via X-ray magnetic circular dichroism photoemission electron microscopy (XMCD-PEEM).[36]

The CEMS measurements were performed using a constant acceleration spectrometer adopted in the UHV system. A small active-area 100 mCi ^{57}Co (Rh) γ-source is placed outside the UHV system and irradiates the sample through a beryllium window at a 54° angle from the sample normal, with the azimuthal angle corresponding to the [1$\bar{1}$0] direction of the W(110) substrate. A large opening channeltron is used as a conversion electron detector. The Mössbauer spectra were analyzed numerically using Voigt lines, which allow consistent implementation of the hyperfine parameter distribution that is an inherent feature of ultra thin films. The isomer shift values are given with respect to metallic α-Fe. CEMS was used to investigate the composition and magnetic properties of the film volume beyond the topmost layers.

The W(110) substrate was cleaned by annealing in oxygen (P_{O_2} = 10^{-6} mbar, T = 1100 °C), followed by flash annealing to 2000 °C under ultrahigh vacuum (UHV) in order to remove the oxygen. The $Fe_{0.7}Ni_{0.3}$ thin films were grown at room temperature (RT) by the co-deposition of Fe and Ni on the W(110) support, with a total film thickness of about 15 ML. In the SPELEEM, the Fe and Ni evaporators were precalibrated by monitoring the completion of their respective pseudomorphic monolayers on W(110) using LEEM and μ-LEED. The pressure during all depositions remained in the low 10^{-10} mbar range. In the CEMS system the Ni and Fe evaporation rate was precalibrated with a quartz crystal monitor, and the films were grown using the ^{57}Fe isotope.

The structure and the stoichiometry of the films were verified with LEED and X-ray photoemission spectroscopy (XPS) at the Fe 3p and Ni 3p core levels, respectively. The XPS result was compared to the value obtained from the ratio of white line intensities at the respective $L_{2,3}$-edge absorption thresholds. The XAS spectra were measured using partial secondary electron photo-emission yield (the kinetic energy range of 1–2 eV) across the Fe and Ni L_3 absorption thresholds, with an estimated maximum penetration depth of 5–10 nm.

The room temperature grown $Fe_{0.7}Ni_{0.3}$ films were observed to retain a uniform bcc crystal structure. The phase separation into μm-sized fcc and bcc regions was induced upon annealing to moderate temperatures (340 °C to 400 °C).[29]

The oxidation was carried out at 200–250 °C using molecular oxygen at a pressure of 1×10^{-6} mbar in a stepwise manner. XPEEM at Ni 3p and Fe 3p core levels, X-ray absorption spectroscopy (XAS-PEEM), μ-LEED and LEEM-IV data were acquired at RT and under UHV after each oxidation step. In XPEEM, the dependence of the photoelectron inelastic mean free path on the electron kinetic energy was used to obtain information on the depth profile of each chemical species.

3. Results

3.1 Phase separation of the $Fe_{0.7}Ni_{0.3}$ thin film

The phase separation at high temperature in $Fe_{0.7}Ni_{0.3}$ films on W(110) has been studied recently from the monolayer limit[28] up to several nanometer thickness.[29] With increasing temperature, firstly Ni segregation at the film surface is observed at about 200 °C, followed by a lateral separation into the micron-sized regions of fcc and bcc phases above 300 °C. At slightly higher temperatures, film dewetting occurs.

Fig. 1a shows the laterally phase-separated surface with fcc (gray) and bcc (bright) regions, as well as some areas (dark)
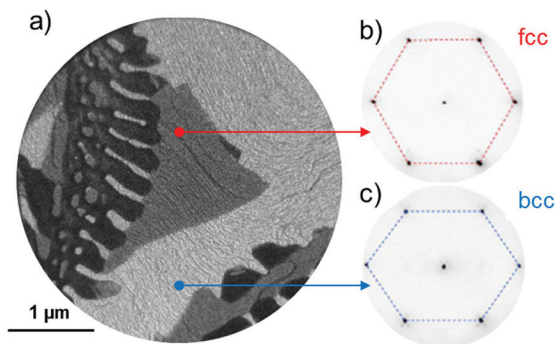
5778 | J. Mater. Chem. C, 2020, **8**, 5777–5785

This journal is © The Royal Society of Chemistry 2020

Fig. 1 (a) LEEM image of the phase separated FeNi film. Electron energy is 21 eV. The μ-LEED patterns from (b) gray (fcc) and (c) bright (bcc) regions are acquired at 65 eV. The finger-like dark regions in the LEEM image correspond to dewetting.

Fig. 2 (a) Evolution of the Fe 3p and Ni 3p core-level intensity ratio as a function of O_2 exposure. (b) Comparison of the XPS spectra at the two core levels acquired upon 0 L and 750 L oxygen exposure. Photon energy is 250 eV.

covered only by a single wetting layer of FeNi due to partial film breakup. The actual Ni compositions in the fcc and bcc phases for the sample in Fig. 1 are found to be in ranges of $x_{fcc} = 0.40 \pm 0.02$ and $x_{bcc} = 0.26 \pm 0.02$, respectively, from an analysis of their corresponding X-ray absorption spectra (XAS) at the respective L-edges. The observed stoichiometry slightly deviates from the previously reported values.[29] This is due to the different thermal treatments the surface was subjected to. In fact, the surface displayed in Fig. 1 was annealed for a shorter period in order to avoid extensive dewetting, and thus it was not fully developed towards the preferred phase compositions. Thus, in different sample preparations, variations in the stoichiometry of the two phases are expected.

3.2 Oxidation

After separation in fcc and bcc regions, the $Fe_{0.7}Ni_{0.3}$ film was exposed to molecular oxygen in incremental steps at 200–250 °C $(P_{O_2} = 1 \times 10^{-6}$ mbar), up to the final exposure of about 3000 L. During oxidation, the change in the surface composition was monitored by probing the Fe and Ni X-ray photoemission core levels, as well as X-ray absorption spectroscopy (XAS) at the Fe and Ni L-edges.

The alloy film surface undergoes dramatic changes upon oxidation, as reflected by the XPS data at a photon energy of 250 eV. The Fe 3p core level shifts to higher binding energy by $\Delta E_B = 2.25$ eV (see Fig. 2b), while the binding energy of the Ni peak remains unchanged, indicating the preferential oxidation of the Fe (both fcc and bcc). At the same time, we find that the Fe 3p (or I_{XPS}^{Fe} in the following) and Ni 3p (I_{XPS}^{Ni}) intensities change progressively with the oxygen dose. In particular, the intensity ratio $I_{XPS}^{Fe}/I_{XPS}^{Ni}$ increases both in fcc and bcc regions as the oxidation proceeds (Fig. 2). Considering that the amount of Fe and Ni in the film is conserved, the change in the photoemission intensity ratio can be attributed to the surface enrichment of Fe, along with the limited inelastic mean free path of photoelectrons.[37] This is in line with the previous observations of Fe surface segregation in Fe–Ni alloys in the presence of oxygen.[30]

The element-selective oxidation is also revealed in the sequence of XAS measurements in Fig. 3, which are less surface
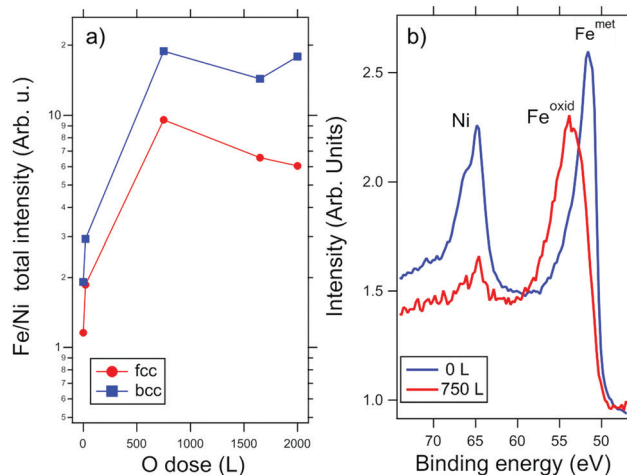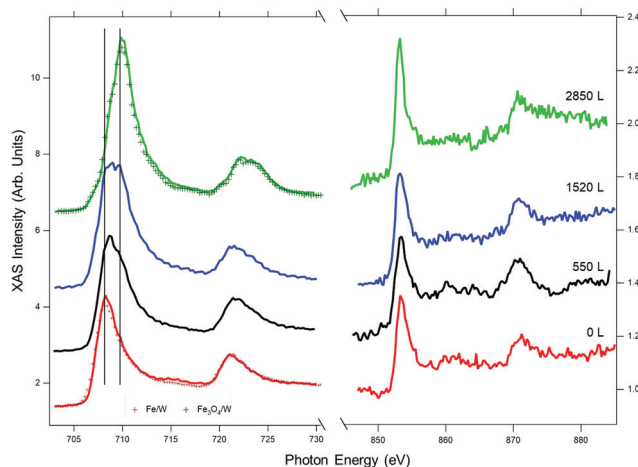

Fig. 3 Integrated XAS measurements at the Fe $L_{2,3}$- and Ni $L_{2,3}$ edges for a $Fe_{0.7}Ni_{0.3}$ thin film upon increasing O_2 exposure. The reference Fe L-edge spectrum of metallic Fe/W and Fe_3O_4/W samples are superimposed to the first and last spectra.

sensitive compared to XPS. The formation of an Fe-oxide layer can be seen in the Fe L-edge spectra by the decrease of the metallic peak intensity (at 707.8 eV) and the appearance of a new peak at 709 eV as well as a smaller component at 710 eV. On the other hand, the Ni spectra remain unchanged, with a single peak at 853 eV, ascribable to metallic Ni. The characteristic shape of the Fe L_3 spectra[38] indicates that the superficial Fe firstly oxidizes to FeO_x (see for instance the spectrum at 550 L). As will be shown below, in the subsequent stages of the oxidation, this layer transforms to Fe_3O_4.

The composition of the film beyond the surface layer was probed using CEMS by averaging over the entire sample. The CEMS spectra at oxygen doses of 250 L and 1650 L are shown in Fig. 4 along with the data from the pristine alloy film surface. Before oxygen exposure, the CEMS spectrum (Fig. 4, top) has a

This journal is © The Royal Society of Chemistry 2020

J. Mater. Chem. C, 2020, **8**, 5777–5785 | **5779**

purely metallic character. The numerical fit shows two components with distinctly different hyperfine parameters. The more intense component, comprising 80% of the spectral intensity component (light gray in Fig. 4), with an average hyperfine magnetic field $\langle B_{hf} \rangle$ = 33.0 T and isomer shift IS = 0.05 mm s^{-1} closely matches the spectrum expected from a bcc FeNi alloy with approximately 75% of Fe.[39] The second component, with a low $\langle B_{hf} \rangle$ = 19.0 T and negative IS = −0.11 mm s^{-1}, is characteristic of an fcc FeNi alloy with approximately 60% Fe.[39] At 250 L dose, the CEMS spectrum shows a predominant metallic component from the FeNi alloy, as well as an oxide component with a non-characteristic widely distributed hyperfine pattern. On the basis of a large positive isomer shift, the latter can be interpreted as the fingerprint of Fe^{2+}, *i.e.* as in a magnetically polarized FeO layer. The oxide contribution accounts for about 15% of the total spectral intensity, suggesting the oxidation of somewhat below 2 ML equivalent of Fe, in agreement with the XPS data.

At an O$_2$ dose of 1650 L, the CEMS spectrum shows that approximately one third of the FeNi remains in the metallic state. As seen in Table 1, the low hyperfine field value (B_{hf} = 28.5 T) of the metallic component compared to that of the pristine film

Table 1 Fit parameters and fit uncertainties for the CEMS spectrum after 1650 L oxygen dose at 250 °C: IS – isomer shift relative to metallic Fe, $\langle B_{hf} \rangle$ – average magnetic hyperfine field

	IS [mm s^{-1}]	$\langle B_{hf} \rangle$ [T]	%
Tetrahedral	0.26 ± 0.02	46.8 ± 0.1	18 ± 1
Octahedral	0.64 ± 0.01	44.1 ± 0.1	26 ± 2
Octa-like	0.63 ± 0.05	38.7 ± 0.9	13 ± 3
Metallic	0.06 ± 0.03	28.5 ± 0.3	29 ± 2
Rest	0.3 ± 0.09	8.1 ± 0.9	14 ± 2

(average B_{hf} = 32.1 T) indicates Ni enrichment within the metallic part, consistent with the segregation and selective oxidation of Fe. The oxide phase is mainly of Fe$_3$O$_4$ character. Compared to the ideal Fe$_3$O$_4$ composition, this oxide shows a deficit of the ideal octahedral sites. Moreover, the low-field tail of the component reveals the presence of a non-stoichiometric Fe–Ni spinel, where Ni cations are located at the octahedral sites. Such a mixed spinel phase could not be detected by surface sensitive XPS and XAS measurements, and most likely is situated in the sub-surface region at the interface between the oxide layer and the metallic alloy.

Finally, a small part of the signal forms a component that cannot easily be attributed to known Fe species. Its significantly lower hyperfine field (B_{hf} = 8.1 T) and its non-zero isomer shift (IS = 0.30 mm s^{-1}) differ from the parameters of metallic Fe, as well as those of the well-defined oxide species. The isomer shift points towards the 3+ oxidation state, whereas the low hyperfine field may result from a lower coordination (*e.g.* at the film surface). This component possibly reflects the disorder induced in the film by mass transport and oxide formation at relatively low temperature.

3.3 Reactivity of the bcc and fcc phases

Spatially resolved measurements were used to characterize the evolution of the bcc and fcc phases in the phase-separated Fe$_{0.7}$Ni$_{0.3}$ film by increasing the oxygen dose in a stepwise manner. The µ-LEED patterns from each region at different stages of oxidation, displayed in Fig. 5, show the formation of symmetry-dependent moiré patterns starting at the lowest dose, which develop into FeO(111) layers on both regions at 1240 L. The weak (2 × 2) pattern at 1700 L, also visible on both phases, indicates the transformation towards an Fe$_3$O$_4$(111) surface.

Importantly, the rate of oxidation as a function of dose is significantly different for the bcc and fcc phases, as reflected in the LEEM IV curve. The XAS spectra were measured using the secondary electron photo-emission yield (in the energy range of 1–2 eV) across the absorption thresholds, with an estimated penetration depth of 5–10 nm as discussed in the ESI.† The changes at low dose appear to take place faster in the bcc region. The higher reactivity of the bcc phase is also confirmed by the XPEEM image at the O 1s core level, which reveals a higher oxygen concentration at the bcc surface at 8.4 L dose as seen in Fig. 6.

We should note that at an O$_2$ dose of about 1250 L, at which the surface is mostly covered with an FeO(111) layer, the fcc–bcc phase boundary has a different contrast in laterally resolved
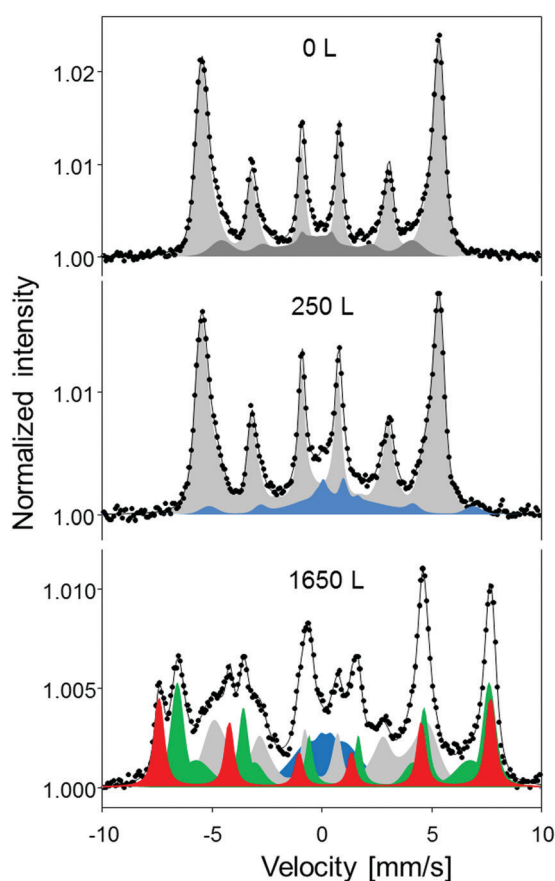
Fig. 4 CEMS spectra of the Fe$_{0.7}$Ni$_{0.3}$ film are shown for varying oxygen dose. The measurement averages over both fcc and bcc phases of the phase-separated alloy film. The spectral components are color-coded: light gray – metallic FeNi; red – the tetrahedral site in the spinel; green – the octahedral site in the spinel; and blue – non-specific oxide components. For the top spectrum of the pristine film the decomposition into bcc-FeNi (light gray) and fcc-FeNi is shown.
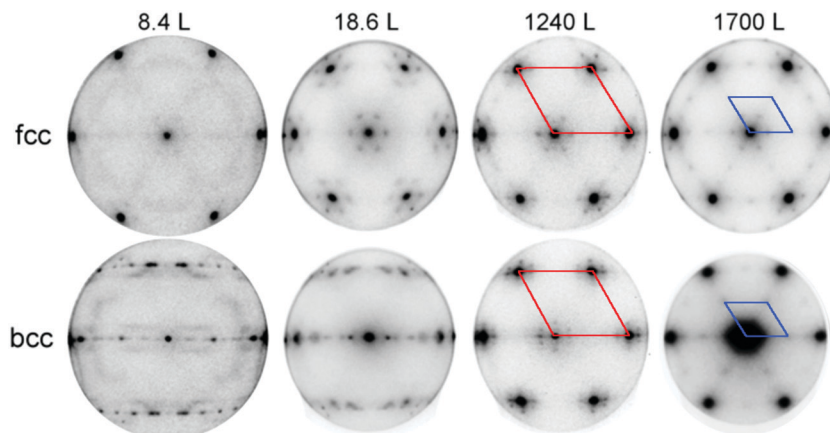
5780 | *J. Mater. Chem. C*, 2020, **8**, 5777–5785

This journal is © The Royal Society of Chemistry 2020

Fig. 5 μ-LEED patterns as a function of oxygen dose for the fcc (top row) and bcc (bottom row) phases present in the phase-separated alloy surface. The electron energy is 45 eV. The unit cell for the FeO and Fe_3O_4 phases is indicated in the image (red and blue lines, respectively); the substrate $[1\bar{1}0]$ direction is along the horizontal axis.
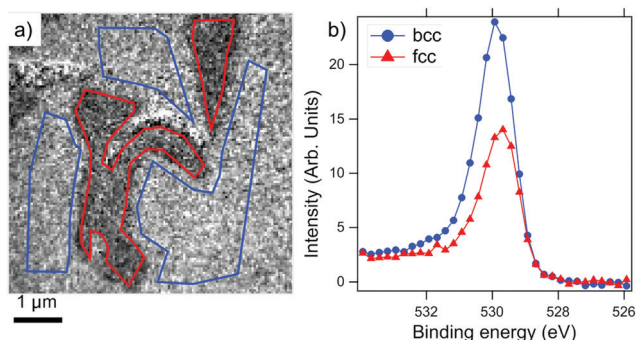

Fig. 6 (a) XPEEM image at the oxygen 1s core level after exposing the phase-separated alloy surface to 8.4 L O_2. The dark (bright) regions, highlighted by the red (blue) contours, correspond to the fcc (bcc) areas. (b) The XPS spectra from the bcc and fcc regions, which are marked on the XPEEM image.

images (see the ESI†). The nature of the border can be identified as Fe_3O_4, based on the O K-edge and Fe L-edge XAS data, as well as the observation of magnetic domains in XMCD-PEEM images at the Fe L_3 edge (also shown in the ESI†). Therefore, we conclude that the boundaries between these two regions are by far the most reactive regions.

In order to deliver a higher O_2 dose than under vacuum, the phase-separated surface was briefly exposed to air at room temperature, followed by annealing at 200 °C in 1.0×10^{-6} mbar oxygen. The resulting surface is chemically mapped by X-ray absorption spectroscopy as shown in Fig. 7. Apart from the large dewetted areas formed during phase separation and recognizable by the dark contrast, the fcc islands are visible as micron-sized elongated regions. The presence of Fe_3O_4 and metallic Ni can be seen both for bcc and fcc regions. The main difference between the two regions is the corresponding white line intensities of the respective elements. The Fe L-edge and O K-edge signals are considerably stronger in the bcc region, whereas the Ni L-edge signal is significantly stronger in the fcc region compared to the bcc areas.

We interpret the different intensities to be due to a considerably thicker FeO_x overlayer on top of the bcc areas. The Ni

XAS signal in the fcc region is quantitatively very similar to the corresponding signal level before oxidation, therefore, we can conclude that the Fe oxide layer on the fcc region is atomically thin and thus it does not cause any discernible screening of the secondary photoelectrons. The magnetic nature of the resulting oxide/metal complex will be the subject of the following section.

3.4 Magnetism

As we have reported in the previous section, it is significantly more difficult to oxidize the fcc Fe–Ni phase in comparison to the bcc phase. Nevertheless, the CEMS and X-ray absorption spectroscopy measurements point to the formation of a magnetite layer over the entire surface upon a sufficient level of oxidation. After air exposure, the magnetic properties of the same $Fe_{0.7}Ni_{0.3}$ film shown in Fig. 7 were investigated using XMCD-PEEM at the Fe and Ni L_3 edges in an element-specific manner.

An XMCD-PEEM image at the Ni L_3 edge is shown in Fig. 8a. Considering that the Ni XAS signal is highly suppressed in the bcc region (see Fig. 7c), the domains can be reliably determined only within the fcc regions. The fcc islands are mostly in a single domain state, with only small variations of the magnetic contrast within individual islands. The absorption peak of Ni predominantly shows metallic nature, thus, we can attain the magnetic contrast to the Fe–Ni alloy underneath the oxide layer.

On the other hand, the XMCD images at the Fe L_3 edge show a more complex photon-energy dependent magnetization map. In Fig. 8b, the XMCD-PEEM image at the photon energy corresponding to metallic Fe (708 eV) reveals the presence of small (less than 100 nm) magnetic domains within the bcc region. The laterally resolved XAS and XMCD spectra at the Fe L_3 edge extracted from these domains are shown in Fig. 8c. The XMCD spectrum is typical of Fe_3O_4 with the negative peaks corresponding to the Fe^{2+} and Fe^{3+} ions at octahedral sites and the positive peak due to the Fe^{3+} ions at tetrahedral sites.[13,40–42] The peaks in the asymmetry spectrum in Fig. 8c are marked by vertical arrows, and the XMCD images at the latter two energies are shown in Fig. 8d and e. Indeed, the small domains within the bcc region appear with weak but inverted contrast at
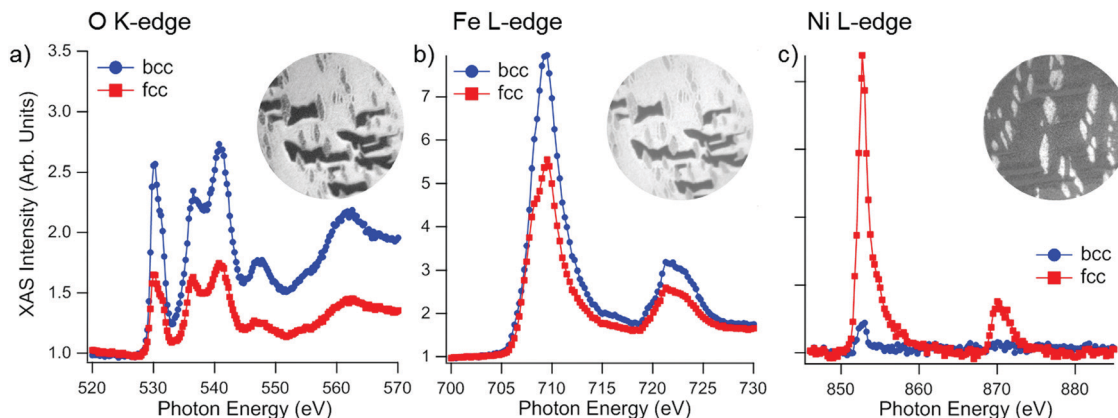
Fig. 7 (a) O K-edge, (b) Fe L-edge, and (c) Ni L-edge XAS spectra from the fcc and bcc regions of a phase-separated $Fe_{0.7}Ni_{0.3}$ film after air exposure followed by annealing at 200 °C in 1×10^{-6} mbar oxygen. The baseline is normalized to unity for all the spectra. The insets show the XPEEM images at the absorption thresholds (for oxygen integrated from 529 to 550 eV; for Fe and Ni at their L_3 edges) normalized pixel-by-pixel to the corresponding pre-edge intensity. The field of view is 5 μm in all XPEEM images. The darkest regions correspond to dewetted areas, whereas the fcc regions appear as vertically elongated islands. Ni spectra are taken from a different region on the same surface.

709.1 eV in comparison to the image at 708.0 eV, while at 709.9 eV the contrast is the same as that at 708.0 eV.

The contribution of the metallic Fe underneath, which is expected to reach a maximum at a photon energy of 708 eV, cannot be unequivocally determined within the bcc regions, as the thick oxide layer suppresses the signal from the metallic alloy underneath. Therefore, the metal–oxide interface in the bcc phase was evaluated for a lower oxygen dose, as shown in the ESI.† For such a thinner oxide layer, we observe an indication for ferromagnetic coupling between Fe_3O_4 and Fe–Ni(bcc).

Instead, in the fcc regions (surrounded by the red contours in Fig. 8 for a clear visualization) the situation is completely different as compared to the bcc areas. A strong contrast is seen at the Fe edge at 708.0 eV (Fig. 8b) coinciding with the XMCD image at the Ni edge at 853.0 eV (Fig. 8a), *i.e.* the relative grayscale in the two images remains the same. At 709.1 eV the XMCD contrast within the fcc islands is the same but much weaker (Fig. 8d). Surprisingly, at 709.9 eV (shown in Fig. 8e) the XMCD contrast inverts in the fcc regions, that is, brighter regions become darker and *vice versa*; this can be seen very clearly looking at the two joint islands on top of the image (highlighted by green circle), but is also observed for all the other fcc regions. This unusual sequence of contrast inversion differs from that of pure Fe_3O_4 (or of a sufficiently thick oxide layer, in this case), for which we would expect the images at 708.0 eV and 709.9 eV to have the same contrast, opposite with respect to the image acquired at 709.1 eV photon energy. A similar reasoning can be applied to the case of pure metallic Fe (or a sufficiently thin oxide layer), which would exhibit high contrast at 708.0 eV, aligned with the Ni edge, and vanishing at higher photon energies. To explain the observed behavior one has to take into account a superposition of contributions from the metallic Fe underneath and the oxide layer above. At a photon energy of 708.0 eV the XMCD signal from the metallic Fe (aligned with that of metallic Ni) dominates and overtakes the Fe_{oct}^{2+} peak from the relatively thin Fe_3O_4 overlayer. At 709.9 eV as seen in Fig. 8e, there is no contribution from

metallic Fe, and the XMCD signal originates solely from the Fe_{oct}^{3+} in Fe_3O_4. The inverted contrast between Fig. 8b and e is indeed direct evidence of antiferromagnetic coupling between the metallic alloy underneath and the oxide layer above. At an intermediate photon energy of 709.1 eV in Fig. 8d, the contrast is thus the same as that of the metallic Fe at 708.0 eV, because both the tails of the metallic XMCD peak and the Fe_{tet}^{3+} oxide peak give the same sign of dichroic asymmetry. Moreover, we note that in any other possible magnetic state of the stack, such as: (i) FM alignment, (ii) thick or (iii) ultrathin Fe_3O_4 layer, and (iv) non-magnetic oxide, the third image should either have the same contrast as the first (cases i and ii) or no magnetic contrast at all (cases iii and iv).

Aside from the magnetic coupling between the metal and oxide layers, considering that the XMCD measurements were carried out with the substrate $[1\bar{1}0]$ direction aligned with the circularly polarized X-ray beam, we can state that at least part of the magnetization lies along this direction. Additional information about the magnetization direction comes from the CEMS measurements. Given the CEMS measurement geometry, the intensity ratio $I_2/I_3 = 0.9$ of the second and third lines in the spectrum of the pristine film (compare Fig. 4) clearly corresponds to the $[1\bar{1}0]$ magnetization direction. Upon oxidation the I_2/I_3 ratio increases to 1.45 for the metallic component, whereas for the spinel components it takes a value of 2, which indicates a tendency of the easy magnetization axis to rotate from $[1\bar{1}0]$ towards $[001]$. The discussion of whether this tendency is due to the abundance of domain walls or whether it indicates a spin reorientation transition is beyond the scope of this work, and it will be the subject of an experimental study with full vectorial mapping of the magnetization.

4. Discussion

In previous sections we have reported the oxidation of the phase-separated $Fe_{0.70}Ni_{0.30}$ film. The main findings can be summarized
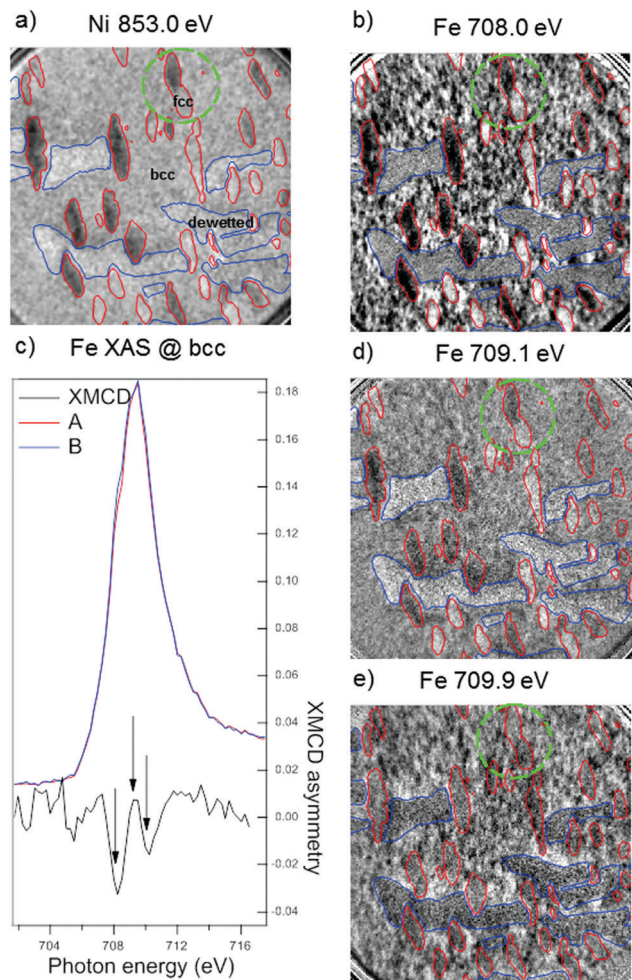
Fig. 8 XMCD-PEEM images of the air-exposed $Fe_{0.7}Ni_{0.3}$ film at (a) Ni L_3 at 853.0 eV, and (b) Fe L_3 at 708.0 eV. (c) Laterally resolved Fe L_3 spectra with circular polarization from dark (A) and bright (B) domains in panel (b) are shown along with the asymmetry between the two spectra (c). Based on the spectrum in (c), XMCD-PEEM images are acquired also at photon energies (d) 709.1 eV and (e) 709.9 eV. In all images, the red lines delineate the fcc regions, whereas the blue lines indicate the dewetted areas. In the asymmetry spectrum, the vertical arrows indicate the photon energies at which the images are acquired.

as: (i) the oxidation proceeds over both fcc and bcc phases with the segregation of Fe at the surface and the formation of an FeO(111) layer, which transforms into Fe_3O_4(111) upon further oxidation; (ii) the small contribution from $Ni_xFe_{3-x}O_4$ in the CEMS data is attributed to a buffer layer between the metallic alloy underneath and the Fe-oxide on top; (iii) in the phase-separated alloy, the fcc region is found to be much less reactive towards oxidation in comparison to the bcc regions; (iv) the magnetic coupling between the metal alloy and the Fe_3O_4 overlayer is found to be antiferromagnetic for the fcc regions; instead the coupling within the bcc regions cannot be unambiguously determined for the heavily oxidized sample.

The first point, which is the formation of an FeO_x layer on top of the Fe-Ni alloy, had been reported long ago, explained by the higher heat of formation of Fe_3O_4 in comparison to NiO.[30] The same work ruled out the formation of a mixed Ni-Fe oxide

below 70% Ni content. Our data confirm the absence of an extensive Ni-Fe-O spinel phase due to the metallic nature of the observed Ni XAS spectrum. Moreover, in Fig. 8c, we show the typical Fe_3O_4 XMCD spectrum, while the literature reports a considerably enhanced Fe_{tet}^{3+} peak in the $Ni_xFe_{3-x}O_4$ XMCD spectrum at the Fe L_3 edge.[43] Thus, $NiFe_2O_4$ contribution to our CEMS data can be attributed to an atomically thin layer restricted to the metal–oxide interface.

The difference in the level of oxidation between the fcc and bcc regions is equally evident both for the lowest and the highest oxygen exposure, as seen from Fig. 6 and 7, respectively. The lower oxidation rate with increasing Ni content in Fe-Ni alloys was reported in the early literature and it was explained to be due to a Ni-rich passivating buffer layer.[31] Nevertheless, our results are obtained from ultrathin films, where the stoichiometry of the buried metal alloy depends sensitively on the amount of Fe segregated at the surface of the Fe-oxide layer. Thus, a thermodynamic consideration comparing the relative energy of different alloy compositions may be relevant in the explanation of the difference in the oxidation rates. In particular, for the fcc $Fe_{1-x}Ni_x$ alloys, the $L1_0$ structure at $x = 0.50$ is identified as the global minimum in energy.[44] Based on this, one may argue that the fcc phase in the phase separated alloy may oppose to release the necessary Fe for the oxide formation beyond a stoichiometry of $Fe_{0.50}Ni_{0.50}$.

In short, the suppressed reactivity of the fcc phase in comparison to the Fe-rich bcc phase may have contributions both from kinetic limitations increasing with Ni content and from energetics favoring a particular alloy stoichiometry. In order to identify which of the two mechanisms is the dominant one, further studies of composition-dependent reactivity in fcc $Fe_{1-x}Ni_x$ ultrathin films near $x = 0.50$ will be necessary.

The magnetization measurements provide direct comparisons between the bcc(110) and fcc(111) films as the support layer for the Fe_3O_4 top layer. Before oxidation both phases in the film display large and uniform magnetic domains. Upon forming the Fe-oxide layer on top, the domain size and distribution are distinctly different for the fcc and bcc phases. The fcc phase retains the single domain state in each fcc island, while the bcc phase breaks into magnetic domains of size below 100 nm, as seen in Fig. 8a and b. The reason for the small domains may be due to a more defective interface between the lattices with different symmetries. Alternatively, the domain morphology may be due to the defect density in the oxide overlayer resulting from the relatively low oxidation temperature or in the alloy underlayer after the removal of a considerable amount of Fe in order to form the relatively thick Fe_3O_4 layer on top.

Regarding the magnetic coupling between the metal support and the oxide overlayer, the fcc regions are coupled antiferromagnetically to the Fe_3O_4 top layer. This behaviour in the fcc regions is different than the reported ferromagnetic coupling between Fe_3O_4 and Ni(111).[20] A similar situation is found for the bcc regions. Contrary to what was observed for Fe_3O_4/Fe(110), we have seen an indication of ferromagnetic coupling at the metal–oxide interface within the bcc(110) regions for a thinner oxide layer, as displayed in the ESI.†

This journal is © The Royal Society of Chemistry 2020

J. Mater. Chem. C, 2020, **8**, 5777–5785 | **5783**

These differences necessarily originate from the details of the interface. The effect of the interface has been documented well in the case of $Fe_3O_4/Fe(110)$, in which the antiferromagnetic coupling was explained by an Fe layer at the interface featuring only 3+ octahedral sites.[45] On the other hand, in $NiFe_2O_4$ the Ni^{2+} ions preferentially replace the Fe^{2+} ions at the octahedral sites.[46] Therefore, the presence of Ni atoms at the oxide–metal interface likely favors a different oxide layer termination, and subsequently may change the spin orientation of the layer coupled to the metal.

We note here that the results summarized above lead to two significant predictions: (i) oxidation of Ni/Fe(110) may help tune the resulting oxide–metal magnetic coupling from antiparallel to parallel depending on the Ni coverage and (ii) based on the opposite coupling observed between bcc and fcc regions, we expect that the magnetic trilayer $Fe_{1-x}Ni_x(fcc)/Fe_3O_4/Fe_{1-y}Ni_y(bcc)$ is a candidate for the observation of large magnetoresistivity based on the half-metallic character of Fe_3O_4.[10]

5. Conclusions

We report on the oxidation of fcc and bcc Fe–Ni phases under identical conditions. In both phases, Fe segregation and its selective oxidation to FeO and Fe_3O_4 are observed. The bcc phase, with its higher Fe content, is shown to be significantly more reactive in comparison to the fcc phase. At the interface between the underlying metal and the FeO_x overlayer, a Ni containing buffer layer is revealed by Mössbauer measurements. The resulting magnetic domains and the metal–oxide magnetic coupling are shown to be distinctly different compared to the coupling between Fe_3O_4 and the elemental constituents of the alloy. Thus, the oxidation of the phase separated Fe–Ni alloy provides information on how the symmetry and interface chemistry modify the magnetic coupling at an oxide–metal interface, and opens up possibilities to tailor the interface properties with applications in mind.

Conflicts of interest

There are no conflicts to declare.

Acknowledgements

References

1 J. M. D. Teresa, A. Barthélémy, A. Fert, J. P. Contour, F. Montaigne and P. Seneor, Role of metal–oxide interface in determining the spin polarization of magnetic tunnel junctions, *Science*, 1999, **286**, 507.

2 S. Ikeda, K. Miura, H. Yamamoto, K. Mizunuma, H. D. Gan, M. Endo, S. Kanai, J. Hayakawa, F. Matsukura and H. Ohno, A perpendicular-anisotropy CoFe-Mgo magnetic tunnel junction, *Nat. Mater.*, 2010, **9**, 721.

3 A. Kozioł-Rachwał, T. Ślezak, K. Matlak, P. Kuświk, M. Urbaniak, F. Stobiecki, L. D. Yao, S. van Dijken and J. Korecki, Tunable magnetic properties of monoatomic metal-oxide Fe/MgO multilayers, *Phys. Rev. B: Condens. Matter Mater. Phys.*, 2014, **90**, 045428.

4 O. Boulle, J. Vogel, H. Yang, S. Pizzini, D. de Souza Chaves, A. Locatelli, T. O. Menteş, A. Sala, L. D. Buda-Prejbeanu, O. Klein, M. Belmeguenai, Y. Roussigné, A. Stashkevich, S. M. Chérif, L. Aballe, M. Foerster, M. Chshiev, S. Auffret, I. M. Miron and G. Gaudin, Room-temperature chiral magnetic skyrmions in ultrathin magnetic nanostructures, *Nat. Nanotechnol.*, 2016, **11**, 449.

5 F. Hellman, A. Hoffmann, Y. Tserkovnyak, G. S. D. Beach, E. E. Fullerton, C. Leighton, A. H. MacDonald, D. C. Ralph, D. A. Arena, H. A. Dürr, P. Fischer, J. Grollier, J. P. Heremans, T. Jungwirth, A. V. Kimel, B. Koopmans, I. N. Krivorotov, S. J. May, A. K. Petford-Long, J. M. Rondinelli, N. Samarth, I. K. Schuller, A. N. Slavin, M. D. Stiles, O. Tchernyshyov, A. Thiaville and B. L. Zink, Interface-induced phenomena in magnetism, *Rev. Mod. Phys.*, 2017, **89**, 025006.

6 J. Coey, Ariando and W. Pickett, Magnetism at the edge: New phenomena at oxide interfaces, *MRS Bull.*, 2013, **38**, 1040–1047.

7 G. Li, G. R. Blake and T. T. M. Palstra, Vacancies in functional materials for clean energy storage and harvesting: the perfect imperfection, *Chem. Soc. Rev.*, 2017, **46**, 1693–1706.

8 Z. Huang, W. Liu, J. Yue, Q. Zhou, W. Zhang, Y. Lu, Y. Sui, Y. Zhai, Q. Chen, S. Dong, J. Wang, Y. Xu and B. Wang, Enhancing the spin orbit coupling in Fe_3O_4 epitaxial thin films by interface engineering, *ACS Appl. Mater. Interfaces*, 2016, **8**, 27353–27359.

9 F. Ozcep, *Earth Sciences History*, 2018, **37**, 1.

10 J.-H. Park, E. Vescovo, H.-J. Kim, C. Kwon, R. Ramesh and T. Venkatesan, Direct evidence for a half-metallic ferromagnet, *Nature*, 1998, **392**, 794.

11 G. S. Parkinson, Iron oxide surfaces, *Surf. Sci. Rep.*, 2016, **71**, 272.

12 N. Spiridis, D. Wilgocka-Ślezak, K. Freindl, B. Figarska, T. Giela, E. Młyńczak, B. Strzelczyk, M. Zajac and J. Korecki, Growth and electronic and magnetic structure of iron oxide films on Pt(111), *Phys. Rev. B: Condens. Matter Mater. Phys.*, 2012, **85**, 075436.

13 M. Monti, B. Santos, A. Mascaraque, O. Rodríguez de la Fuente, M. A. Niño, T. O. Menteş, A. Locatelli, K. F. McCarty, J. F. Marco and J. de la Figuera, Magnetism in nanometer-thick magnetite, *Phys. Rev. B: Condens. Matter Mater. Phys.*, 2012, **85**, 020404.

14 M. Monti, B. Santos, A. Mascaraque, O. Rodríguez de la Fuente, M. A. Niño, T. O. Menteş, A. Locatelli, K. F. McCarty, J. F. Marco and J. de la Figuera, Oxidation pathways in bicomponent ultrathin iron oxide films, *J. Phys. Chem. C*, 2012, **116**, 11539–11547.

15 F. Genuzio, A. Sala, T. Schmidt, D. Menzel and H.-J. Freund, Interconversion of α-Fe_2O_3 and Fe_3O_4 thin films: Mechanisms,

5784 | *J. Mater. Chem. C*, 2020, **8**, 5777–5785

This journal is © The Royal Society of Chemistry 2020

morphology, and evidence for unexpected substrate participation, *J. Phys. Chem. C*, 2014, **118**, 29068.

16 F. Genuzio, A. Sala, T. Schmidt, D. Menzel and H.-J. Freund, Phase transformations in thin iron oxide films: Spectromicroscopic study of velocity and shape of the reaction fronts, *Surf. Sci.*, 2016, **648**, 177.

17 D. Tripathy and A. O. Adeyeye, Giant magnetoresistance in half metallic Fe_3O_4 based, *J. Appl. Phys.*, 2007, **101**, 09J505.

18 S. v. Dijken, X. Fain, S. M. Watts and J. M. D. Coey, Negative magnetoresistance in Fe_3O_4 AuFe spin valves, *Phys. Rev. B: Condens. Matter Mater. Phys.*, 2004, **70**, 052409.

19 K. Omori, T. Kawai, N. Takahashi, T. Yanase, T. Shimada and T. Nagahama, The magnetic properties of Fe_3O_4/nonmagnetic metal/Fe hybrid systems, *Appl. Phys. Lett.*, 2017, **110**, 212402.

20 W. Xiao, W. Song, T. S. Herng, Q. Qin, Y. Yang, M. Zheng, X. Hong, Y. P. Feng and J. Ding, Novel room-temperature spin-valve-like magnetoresistance in magnetically coupled nano-column Fe_3O_4/Ni heterostructure, *Nanoscale*, 2016, **8**, 15737.

21 W. F. McDonough and S. S. Sun, The composition of the Earth, *Chem. Geol.*, 1995, **120**, 223.

22 B. D. Cullity and C. D. Graham, *Introduction to Magnetic Materials*, Wiley-IEEE Press, 2008.

23 B. Dieny, V. S. Speriosu, S. Metin, S. S. P. Parkin, B. A. Gurney, P. Baumgart and D. R. Wilhoit, Magnetotransport properties of magnetically soft spin valve structures, *J. Appl. Phys.*, 1991, **69**, 4774–4779.

24 B. Dieny, V. S. Speriosu, S. S. P. Parkin, B. A. Gurney, D. R. Wilhoit and D. Mauri, Giant magnetoresistive in soft ferromagnetic multilayers, *Phys. Rev. B: Condens. Matter Mater. Phys.*, 1991, **43**, 1297–1300.

25 K. B. Reuter, D. B. Williams and J. I. Goldstein, Determination of the Fe/Ni phase diagram below 400 °C, *Metall. Trans. A*, 1989, **20**, 711.

26 C. W. Yang, D. B. Williams and J. I. Goldstein, A revision of the Fe–Ni phase diagram at low temperatures <400 °C, *J. Phase Equilib.*, 1996, **17**, 522.

27 B. Glaubitz, S. Buschhorn, F. Brüssing, R. Abrudan and H. Zabel, Development of magnetic moments in $Fe_{1-x}Ni_x$-alloys, *J. Phys.: Condens. Matter*, 2011, **23**, 254210.

28 T. O. Menteş, A. Sala, A. Locatelli, E. Vescovo, J. M. Ablett and M. A. Niño, Phase coexistence in two-dimensional $Fe_{0.70}Ni_{0.30}$ films on W(110), *e-J. Surf. Sci. Nanotechnol.*, 2015, **13**, 256.

29 T. O. Menteş, N. Stojić, E. Vescovo, J. M. Ablett, M. A. Niño and A. Locatelli, Vacancy-mediated fcc/bcc phase separation in $Fe_{1-x}Ni_x$ ultrathin films, *Phys. Rev. B*, 2016, **94**, 085402.

30 K. Wandelt and G. Ertl, Electron spectroscopic studies of the oxidation of Fe/Ni alloys, *Surf. Sci.*, 1976, **55**, 403.

31 G. R. Wallwork, The oxidation of alloys, *Rep. Prog. Phys.*, 1976, **39**, 401.

32 A. Locatelli, L. Aballe, T. O. Menteş, M. Kiskinova and E. Bauer, Photoemission electron microscopy with chemical sensitivity: SPELEEM methods and applications, *Surf. Interface Anal.*, 2006, **38**, 1554.

33 E. Bauer, *Surface Microscopy with Low-Energy Electrons*, Springer-Verlag, New York, 2014.

34 A. Locatelli and E. Bauer, Recent advances in chemical and magnetic imaging of surfaces and interfaces by XPEEM, *J. Phys.: Condens. Matter*, 2008, **20**, 093002.

35 T. O. Menteş, G. Zamborlini, A. Sala and A. Locatelli, Cathode lens spectromicroscopy: methodology and applications, *Beilstein J. Nanotechnol.*, 2014, **5**, 1873.

36 C. M. Schneider and G. Schönhense, Investigating surface magnetism by means of photoexcitation electron emission microscopy, *Prog. Rep. Phys.*, 2002, **65**, R1785.

37 S. Tanuma, C. J. Powell and D. R. Penn, Calculations of electron inelastic mean free paths. IX. data for 41 elemental solids over the 50 eV to 30 keV range, *Surf. Interface Anal.*, 2011, **43**, 689–713.

38 W. Weiss and W. Ranke, Surface chemistry and catalysis on well-defined epitaxial iron-oxide layers, *Prog. Surf. Sci.*, 2002, **70**, 1.

39 J. Restrepo, G. A. Pérez Alcázar and A. Bohórquez, Description in a local model of the magnetic field distributions of Fe_xNi_x disordered alloys, *J. Appl. Phys.*, 1997, **81**, 4101–4103.

40 P. Kuiper, B. Searle, L.-C. Duda, R. Wolf and P. Van Der Zaag, Fe $L_{2,3}$ linear and circular magnetic dichroism of Fe_3O_4, *J. Electron Spectrosc. Relat. Phenom.*, 1997, **86**, 107–113.

41 F. Schedin, P. Morrall, V. Petrov, S. Case, M. Thomas, E. Dudzik, G. van der Laan and G. Thornton, Magnetic properties of ultrathin epitaxial Fe_3O_4 films on Pt(111), *J. Magn. Magn. Mater.*, 2000, **211**, 266–270.

42 H.-J. Kim, J.-H. Park and E. Vescovo, Oxidation of the Fe(110) surface: An Fe_3O_4(111)/Fe(110) bilayer, *Phys. Rev. B: Condens. Matter Mater. Phys.*, 2000, **61**, 15284.

43 A. Mandziak, J. de la Figuera, S. Ruiz-Gómez, G. D. Soria, L. Pérez, P. Prieto, A. Quesada, M. Foerster and L. Aballe, Structure and magnetism of ultrathin nickel-iron oxides grown on Ru(0001) by high-temperature oxygen-assisted molecular beam epitaxy, *Sci. Rep.*, 2018, **8**, 17980.

44 S. V. Barabash, R. V. Chepulskii, V. Blum and A. Zunger, First-principles determination of low-temperature order and ground states of Fe–Ni, Fe–Pd, and Fe–Pt, *Phys. Rev. B: Condens. Matter Mater. Phys.*, 2009, **80**, 220201.

45 H.-J. Kim, J.-H. Park and E. Vescovo, Fe_3O_4(111)/Fe(110) magnetic bilayer: Electronic and magnetic properties at the surface and interface, *Phys. Rev. B: Condens. Matter Mater. Phys.*, 2000, **61**, 15288.

46 G. van der Laan, C. M. B. Henderson, R. A. D. Pattrick, S. S. Dhesi, P. F. Schofield, E. Dudzik and D. J. Vaughan, Orbital polarization in $NiFe_2O_4$ measured by Ni-2p X-ray magnetic circular dichroism, *Phys. Rev. B: Condens. Matter Mater. Phys.*, 1999, **59**, 4314.

This journal is © The Royal Society of Chemistry 2020

J. Mater. Chem. C, 2020, **8**, 5777–5785 | **5785**